Evaluation of debonding strength of single lap joint by the intensity of singular stress field

IOP Conf. Series: Journal of Physics: Conf. Series **842** (2017) 012078 doi:10.1088/1742-6596/842/1/012078

Evaluation of debonding strength of single lap joint by the intensity of singular stress field

Tatsujiro Miyazaki[1] **and Nao-Aki Noda**[2]

[1]University of the Ryukyus, 1 Senbaru, Nishihara-cho, Nakagami-gun, Okinawa 903-0213, Japan

[2]Kyushu Institute of Technology, 1-1 Sensui-cho, Tobata-ku, Kitakyushu-shi, Fukuoka 804-8550, Japan

E-mail: t-miya@tec.u-ryukyu.ac.jp

Abstract. In this paper, the similarity of the singular stress field of the single lap joint (SLJ) is discussed to evaluate the debonding fracture by the intensity of the singular stress field (ISSF). The practical method is proposed for analyzing the ISSF for the SLJ. The analysis method focuses on the FEM stress at the interface end by applying the same mesh pattern to the unknown and reference models. It is found that the independent technique useful for the bonded plate and butt joint cannot be applied to the SLJ because the singular stress field of the SLJ consists of two singular stress terms. The FEM stress is divided to two FEM stresses by applying the unknown and reference models to different minimum element sizes. Then, the practicality of the present method is examined by applying to the previous tensile test results of the SLJ composed of the aluminum alloy and the epoxy resin. The ISSFs for the SLJ were calculated by changing the adhesive thickness t_2 and the overlap length l_2. In the case of the SLJ with 225 mm in total length and 7 mm in adherend thickness, it was found that the similar singular stress fields are formed in the range of $0.15\,\text{mm} \leq t_2 \leq 0.9\,\text{mm}$ and $15\,\text{mm} \leq l_2 \leq 50\,\text{mm}$. It is shown that the critical ISSFs at the fracture are constant in the range.

1. Introduction

The intensity of singular stress field (ISSF) is useful for evaluating the debonding strength [1–4]. Generally, the ISSF cannot be calculated directly by the finite element method (FEM) [5–8]. The authors proposed the method for calculating the ISSF easily and accurately by the FEM [3, 4]. The method does not require the complex calculation and can be applied to various bonded structures [9–12]. In the previous studies, the butt joint was analyzed under all material combination by using the bonded plate as the reference solution [3, 4]. The singular stress field of the butt joint is expressed with a singular stress term. On the other hand, for many material combinations, the singular stress field of the single lap joint (SLJ) consists of two singular stress terms and is not discussed sufficiently. The similarity of the singular stress field needs be discussed to evaluate the debonding strength by the ISSF [10, 13]. The method for analyzing two ISSFs easily and conveniently is required.

In this paper, the practical method for calculating two ISSFs for SLJ from the stress at the interface end by FEM is proposed. When the FE analyses are performed on the reference and unknown models under the same mesh patter and the same material combination, the ratio of the FEM stresses at the interface end of the unknown model to that of the reference model

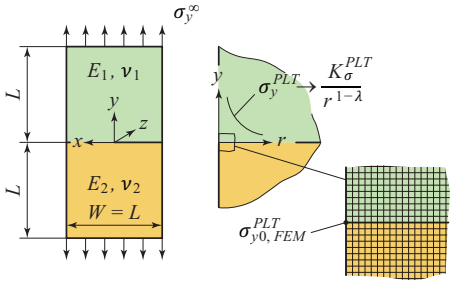

Figure 1. Bonded plate used as the reference model.

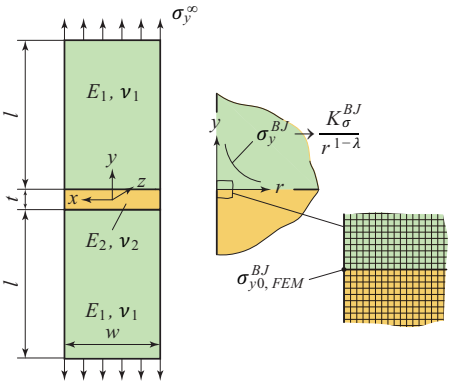

Figure 2. Butt joint used as the unknown model.

corresponds to the ratio of the ISSF of the unknown model to that of the reference model. Since the singular stress field of the SLJ consists on two singular terms, the sum of two FEM stresses is output as the nodal solution. Therefore, the FEM stress is divided to two FEM stresses by applying the unknown and reference models to different minimum element sizes. Then, two ISSFs are calculated by the divided FEM stresses. Then, the present method is applied to the previous experimental results of the SLJ. The similarity of the singular stress field and the debonding fracture criterion are discussed.

2. Mesh-independent technique useful for evaluating the ISSF for butt joint

The authors proposed the method for calculating the ISSF for the butt joint (Fig. 1) accurately by using the ISSF for the bonded plate (Fig. 2) as the reference solution [3, 4]. The real singular stresses of the bonded plate and the butt joint, σ_{ij}^{PLT} and σ_{ij}^{BJ}, are given by the following equations, respectively.

$$\sigma_{ij}^{PLT} = K_{\sigma_{ij}}^{PLT}/r^{1-\lambda} \tag{1}$$

$$\sigma_{ij}^{BJ} = K_{\sigma_{ij}}^{BJ}/r^{1-\lambda} \tag{2}$$

Here, r is the distance on the interface from the corner edge, λ is the singular index, $K_{\sigma_{ij}}^{PLT}$ and $K_{\sigma_{ij}}^{BJ}$ are ISSFs for the bonded plate and the butt joint, respectively. When the FE analyses are performed on the bonded plate and the butt joint under the same mesh pattern and the same material combination, the ratio of the FEM stresses, $\sigma_{ij0,FEM}^{BJ}/\sigma_{ij0,FEM}^{PLT}$, corresponds to the ratio of the ISSFs, $K_{\sigma_{ij}}^{BJ}/K_{\sigma_{ij}}^{PLT}$, as follows [3, 4].

$$\frac{K_{\sigma_{ij}}^{BJ}}{K_{\sigma_{ij}}^{PLT}} = \frac{\lim_{r\to 0} r^{1-\lambda}\sigma_{ij}^{BJ}}{\lim_{r\to 0} r^{1-\lambda}\sigma_{ij}^{PLT}} = \lim_{r\to 0}\frac{r^{1-\lambda}\sigma_{ij}^{BJ}}{r^{1-\lambda}\sigma_{ij}^{PLT}} = \lim_{r\to 0}\frac{\sigma_{ij}^{BJ}}{\sigma_{ij}^{PLT}} \simeq \frac{\sigma_{ij0,FEM}^{BJ}}{\sigma_{ij0,FEM}^{PLT}} \tag{3}$$

The real singular stress of the SLJ is given by the following equation under many material combinations [10, 13].

$$\sigma_{ij}^{SLJ}(r) = \frac{K_{\sigma_{ij},\lambda_1}^{SLJ}}{r^{1-\lambda_1}} + \frac{K_{\sigma_{ij},\lambda_2}^{SLJ}}{r^{1-\lambda_2}} = \frac{K_{\sigma_{ij},\lambda_1}^{SLJ}}{r^{1-\lambda_1}}\left(1 + \frac{C_{\sigma_{ij}}^{SLJ}}{r^{\lambda_1-\lambda_2}}\right),\ C_{\sigma_{ij}}^{SLJ} = \frac{K_{\sigma_{ij},\lambda_2}^{SLJ}}{K_{\sigma_{ij},\lambda_1}^{SLJ}} \tag{4}$$

Here, λ_1 and λ_2 ($\lambda_1 < \lambda_2$) are singular indexes, $K_{\sigma_{ij},\lambda_1}^{SLJ}$ and $K_{\sigma_{ij},\lambda_2}$ are the ISSFs. The FEM stresses which correspond to $K_{\sigma_{ij},\lambda_1}^{SLJ}/r^{1-\lambda_1}$ and $K_{\sigma_{ij},\lambda_2}^{SLJ}/r^{1-\lambda_2}$ are denoted with $\sigma_{ij0,FEM,\lambda_1}^{SLJ}$ and

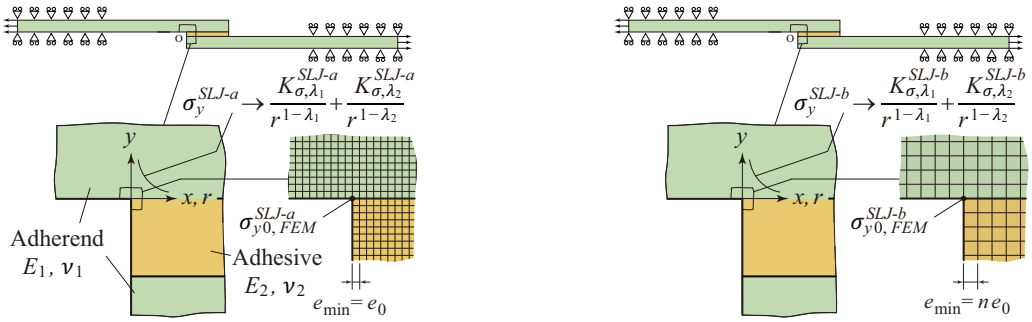

(a) Fine mesh model with minimum element size $e_{\min} = e_0$

(b) Coarse mesh model with minimum element size $e_{\min} = n\,e_0$

Figure 3. Schematic illustration of SLJ models

$\sigma_{ij0,FEM,\lambda_2}^{SLJ}$, respectively. The $\sigma_{ij0,FEM}^{SLJ}$ is expressed with $(\sigma_{ij0,FEM,\lambda_1}^{SLJ} + \sigma_{ij0,FEM,\lambda_2}^{SLJ})$ and is governed by the $\sigma_{ij0,FEM,\lambda_1}^{SLJ}$ because of $\lambda_1 < \lambda_2$. Therefore, only ISSF ratio $K_{\sigma_{ij},\lambda_1}^{SLJ}/K_{\sigma_{ij},\lambda_1}^{SLJ*}$ is determined by the FEM stress ratio $\sigma_{ij0,FEM}^{SLJ}/\sigma_{ij0,FEM}^{SLJ*}$ as follows [10, 13].

$$\frac{K_{\sigma_{ij},\lambda_1}^{SLJ}}{K_{\sigma_{ij},\lambda_1}^{SLJ*}} = \frac{\lim_{r\to 0} r^{1-\lambda_1}\sigma_{ij}^{SLJ}}{\lim_{r\to 0} r^{1-\lambda_1}\sigma_{ij}^{SLJ*}} = \lim_{r\to 0}\frac{r^{1-\lambda_1}\sigma_{ij}^{SLJ}}{r^{1-\lambda_1}\sigma_{ij}^{SLJ*}} = \lim_{r\to 0}\frac{\sigma_{ij}^{SLJ}}{\sigma_{ij}^{SLJ*}} \simeq \frac{\sigma_{ij0,FEM,\lambda_1}^{SLJ}}{\sigma_{ij0,FEM,\lambda_1}^{SLJ*}} \simeq \frac{\sigma_{ij0,FEM}^{SLJ}}{\sigma_{ij0,FEM}^{SLJ*}} \tag{5}$$

The $K_{\sigma_{ij},\lambda_2}^{SLJ}/K_{\sigma_{ij},\lambda_1}^{SLJ}$ is necessary to discuss the similarity of the singular stress field. However, the $K_{\sigma_{ij},\lambda_2}^{SLJ}/K_{\sigma_{ij},\lambda_2}^{SLJ*}$ cannot be calculated from the FEM stress ratio.

3. Mesh-independent technique useful for evaluating the ISSF for SLJ

3.1. Division of the FEM stress

Figure 3 shows the schematic illustrations of the single lap joint models. The model (a) is subdivided by the minimum element size $e_{\min} = e_0$. The FEM stress at the interface end and the ISSF are denoted with $\sigma_{ij0,FEM}^{SLJ\text{-}a} = \sigma_{ij0,FEM}^{SLJ}$ and $K_{\sigma_{ij},\lambda_k}^{SLJ\text{-}a} = K_{\sigma_{ij},\lambda_k}^{SLJ}$, respectively. The model (b) is as large as the model (a) and subdivided by $e_{\min} = ne_0$. The FEM stress at the interface end and the ISSF are denoted with $\sigma_{ij0,FEM}^{SLJ\text{-}b} = \sigma_{ij0,FEM}^{SLJ}|_{e_{\min}=n\,e_0}$ and $K_{\sigma_{ij},\lambda_k}^{SLJ\text{-}b}$, respectively.

The FEM stress of the model (a), $\sigma_{ij0,FEM}^{SLJ}$, is expressed as follows.

$$\sigma_{ij0,FEM}^{SLJ} = \sigma_{ij0,FEM,\lambda_1}^{SLJ} + \sigma_{ij0,FEM,\lambda_2}^{SLJ} \tag{6}$$

The $\sigma_{ij0,FEM}^{SLJ}$ has to be divided into $\sigma_{ij0,FEM,\lambda_1}^{SLJ}$ and $\sigma_{ij0,FEM,\lambda_2}^{SLJ}$ in order to calculate the $K_{\sigma_{ij},\lambda_k}^{SLJ}$.

Since the minimum element size of the model (b) is n times as large as that of the model (a), the FEM stress of the model (b), $\sigma_{ij0,FEM}^{SLJ}|_{e_{\min}=n\,e_0}$, is also expressed as follows [14, 15].

$$\begin{aligned}\sigma_{ij0,FEM}^{SLJ}|_{e_{\min}=n\,e_0} &= \sigma_{ij0,FEM,\lambda_1}^{SLJ}|_{e_{\min}=n\,e_0} + \sigma_{ij0,FEM,\lambda_2}^{SLJ}|_{e_{\min}=n\,e_0} \\ &= \frac{\sigma_{ij0,FEM,\lambda_1}^{SLJ}}{n^{1-\lambda_1}} + \frac{\sigma_{ij0,FEM,\lambda_2}^{SLJ}}{n^{1-\lambda_2}}\end{aligned} \tag{7}$$

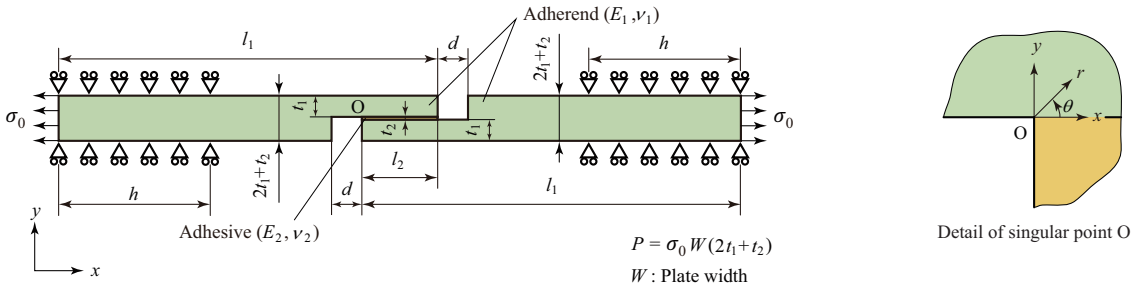

Figure 4. Schematic illustration of the thick adherend single lap joint

When the simultaneous equations (6) and (7) are solved on the $\sigma^{SLJ}_{ij0,FEM,\lambda_1}$ and $\sigma^{SLJ}_{ij0,FEM,\lambda_2}$, the following equations are obtained.

$$\sigma^{SLJ}_{ij0,FEM,\lambda_1} = \frac{\sigma^{SLJ}_{ij0,FEM}}{1-n^{\lambda_1-\lambda_2}} - \frac{\sigma^{SLJ}_{ij0,FEM}\big|_{e_{\min}=n\,e_0}}{n^{\lambda_2-1}-n^{\lambda_1-1}} \tag{8}$$

$$\sigma^{SLJ}_{ij0,FEM,\lambda_2} = -\frac{\sigma^{SLJ}_{ij0,FEM}}{1-n^{\lambda_2-\lambda_1}} + \frac{\sigma^{SLJ}_{ij0,FEM}\big|_{e_{\min}=n\,e_0}}{n^{\lambda_2-1}-n^{\lambda_1-1}} \tag{9}$$

3.2. Mesh-independent technique

The ratio of the ISSFs can be obtained from the ratios of the FEM stresses divided by Eqs. (8) and (9) as follows.

$$\frac{K^{SLJ}_{\sigma_{y0},\lambda_1}}{K^{SLJ*}_{\sigma_{y0},\lambda_1}} = \frac{\sigma^{SLJ}_{y0,FEM,\lambda_1}}{\sigma^{SLJ*}_{y0,FEM,\lambda_1}}, \quad \frac{K^{SLJ}_{\sigma_{y0},\lambda_2}}{K^{SLJ*}_{\sigma_{y0},\lambda_2}} = \frac{\sigma^{SLJ}_{y0,FEM,\lambda_2}}{\sigma^{SLJ*}_{y0,FEM,\lambda_2}} \tag{10}$$

As shown in Eq. (10), the ISSFs for the unknown model can be determined by those for the only one reference model. That is the utmost advantage obtained by dividing the FEM stresses.

4. Application to the experimental result

4.1. Experimental results used in the analysis

The experimental result of the thick adherend SLJ as shown in Fig. 4 by Park et al [16] is used. In the experiment, the adherend and adhesive are aluminum alloy 6061-T6 (Young's modulus $E_1 = 68.9\,\mathrm{GPa}$, Poisson's ratio $\nu_1 = 0.3$) and epoxy resin ($E_2 = 4.2\,\mathrm{GPa}$, $\nu_2 = 0.45$), respectively. $(2l_1 - l_2) = 225\,\mathrm{mm}$, $t_1 = 7\,\mathrm{mm}$ and $h = 37.5\,\mathrm{mm}$ are set. The adhesive thickness t_2 is varied from 0.15 mm to 0.9 mm. The overlap length l_2 is vaired from 15 mm to 50 mm.

Figure 5 shows the fracture load P_{af} under (a) t_2 constant condition and (b) l_2 constant condition. The P_{af} increases with increasing the l_2 as shown in Fig. 5(a). Then, the P_{af} is almost independent of the t_2 under l_2 constant condition. Figure 6 shows the average shear stress at the fracture, $\tau_c = P_{af}/(l_2 W)$, obtained from Fig. 5(a). When $l_2 < 15\,\mathrm{mm}$, the τ_c becomes constant at about 28.7 MPa. When the overlap length is short, the cohesive fracture occurs and the τ_c becomes constant. In this study, it is supposed that debonding fracture occurs when $l_2 > 15\,\mathrm{mm}$.

4.2. Similarity of the singular stress field and debonding fracture criterion

Figure 4 shows the schematic illustration of the analysis model. Dundurs' parameters are $\alpha = -0.8699$ and $\beta = -0.06642$ [10, 13]. The SLJ has two different real singular indexes $\lambda_1 = 0.6062$ and $\lambda_2 = 0.9989$ at point O. In this analysis, all models were subdivided by the same mesh pattern (Fig. 7). The minimum element size $e_{\min}$ is changed to confirme the mesh

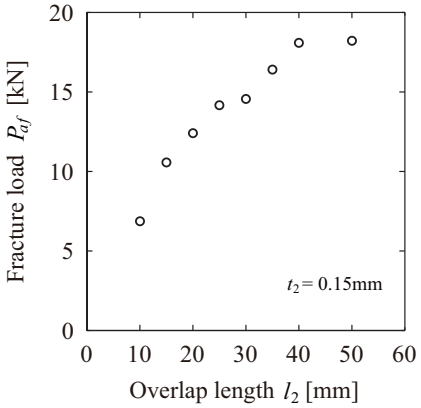

(a) Relationship between P_{af} and l_2 under $t_2 = 0.15\,\mathrm{mm}$

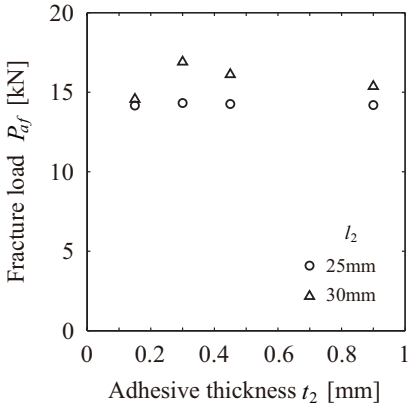

(b) Relationship between P_{af} and t_2 under $l_2 = 25\,\mathrm{mm}$ and $30\,\mathrm{mm}$

Figure 5. Experimental fracture load P_{af} of the specimens in Fig. 4 by Park et al [16]

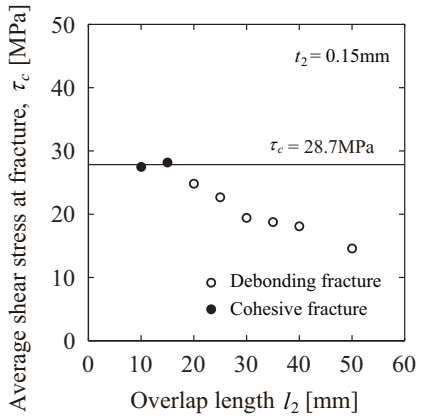

Figure 6. Avarage shear stress at fracture, $\tau_c = P_{af}/(l_2 W)$, obtained from Fig. 5(a) [10, 13]

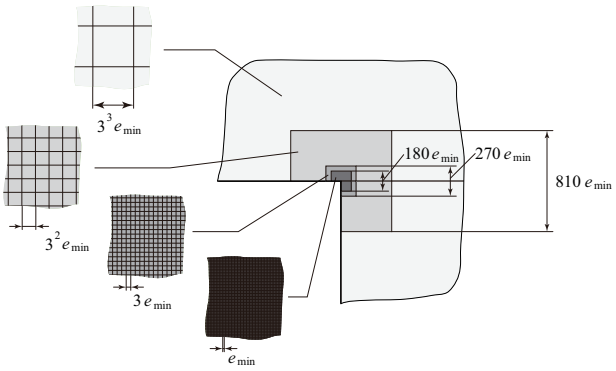

Figure 7. Mesh pattern near the interface end.

independency. $(e_{\min}, ne_{\min}) = (3^{-14}, 3^{-13})$ and $(3^{-13}, 3^{-12})$ are used.

Table 1 shows the FEM stresses of the models with $(l_2, t_2) = (25, 0.15)$, $(50, 0.15)$ and $(25, 0.90)$. The FEM stresses are quite different depending on the mesh size $e_{\min}$. Table 2 shows the $K^{SLJ}_{\sigma_{ij0},\lambda_1}/K^{SLJ*}_{\sigma_{ij0},\lambda_1}$ and the $K^{SLJ}_{\sigma_{ij0},\lambda_2}/K^{SLJ*}_{\sigma_{ij0},\lambda_2}$ obtained from the FEM stress in Table 1, where the specimen A25 model with $(l_2, t_2) = (25, 0.15)$ is used as the reference solution and $*$ is added in the superscript. The $K^{SLJ}_{\sigma_{ij0},\lambda_1}/K^{SLJ*}_{\sigma_{ij0},\lambda_1}$ by the present method is independent of the mesh size $e_{\min}$ and has the same value as the $K^{SLJ}_{\sigma_{ij0},\lambda_1}/K^{SLJ*}_{\sigma_{ij0},\lambda_1}$ by th RWCIM [10]. The $K^{SLJ}_{\sigma_{ij0},\lambda_2}/K^{SLJ*}_{\sigma_{ij0},\lambda_2}$ are little different depending on the $e_{\min}$. That is because the $|\sigma^{SLJ}_{ij0,FEM,\lambda_2}|$ is much smaller than the $|\sigma^{SLJ}_{ij0,FEM,\lambda_1}|$. Since the $K^{SLJ}_{\sigma_{x0},\lambda_2}/K^{SLJ*}_{\sigma_{x0},\lambda_2}$ by the present method has the same value as the $K^{SLJ}_{\sigma_{ij0},\lambda_2}/K^{SLJ*}_{\sigma_{ij0},\lambda_2}$ by th RWCIM, it is found that the FEM stress in the x direction on the material 1 is the most suitable for the present method in this material combination.

Figure 8 shows the $K^{SLJ}_{\sigma_{ij0},\lambda_1}/K^{SLJ*}_{\sigma_{ij0},\lambda_1}$ and the $K^{SLJ}_{\sigma_{ij0},\lambda_2}/K^{SLJ*}_{\sigma_{ij0},\lambda_2}$ obtained by changing the l_2 and the t_2 variously. When $0.15\,\mathrm{mm} \le t_2 \le 0.9\,\mathrm{mm}$ and $15\,\mathrm{mm} \le l_2 \le 50\,\mathrm{mm}$, the $K^{SLJ}_{\sigma_{ij0},\lambda_1}/K^{SLJ*}_{\sigma_{ij0},\lambda_1}$ and the $K^{SLJ}_{\sigma_{ij0},\lambda_2}/K^{SLJ*}_{\sigma_{ij0},\lambda_2}$ decrease linearly with increasing the l_2. Figure 9 shows the $C^{SLJ}_{\sigma_{ij0}}/C^{SLJ*}_{\sigma_{ij0}}$ obtained from the $K^{SLJ}_{\sigma_{ij0},\lambda_1}/K^{SLJ*}_{\sigma_{ij0},\lambda_1}$ and the $K^{SLJ}_{\sigma_{ij0},\lambda_2}/K^{SLJ*}_{\sigma_{ij0},\lambda_2}$ in Fig. 8.

Table 1. Mesh-dependent singular FEM stress at the interface end.

Model (l_2, t_2)	e_0	$\sigma^{SLJ}_{x0,FEM}$ $[=\sigma^{SLJ}_{x0,FEM,\lambda_1}+\sigma^{SLJ}_{x0,FEM,\lambda_2}]$ Mat. 1	Mat. 2	$\sigma^{SLJ}_{x0,FEM}\vert_{e_{\min}=n\,e_0}$ Mat. 1	Mat. 2	$\sigma^{SLJ}_{y0,FEM}$ $[=\sigma^{SLJ}_{y0,FEM,\lambda_1}$ $+\sigma^{SLJ}_{y0,FEM,\lambda_2}]$	$\sigma^{SLJ}_{y0,FEM}\vert_{e_{\min}=n\,e_0}$	$\tau^{SLJ}_{xy0,FEM}$ $[=\tau^{SLJ}_{xy0,FEM,\lambda_1}$ $+\tau^{SLJ}_{xy0,FEM,\lambda_2}]$	$\tau^{SLJ}_{xy0,FEM}\vert_{e_{\min}=n\,e_0}$
A25 $(25, 0.15)$	3^{-14}	1219.634 $[=1212.633$ $+7.001]$	2018.765 $[=2018.660$ $+0.105]$	793.7081	1309.743	1453.725 $[=1454.046$ $-0.321]$	943.0149	-461.4383 $[=-461.4974$ $+0.0591]$	-299.3449
	3^{-13}	793.7081 $[=786.7254$ $+6.9827]$	1309.743 $[=1309.683$ $+0.060]$	517.3754	405.0707	943.0149 $[=943.3633$ $-0.3485]$	611.6741	-299.3449 $[=-299.4065$ $+0.0616]$	-194.1832
A50 $(50, 0.15)$	3^{-14}	927.7130 $[=922.2484$ $+5.4646]$	1535.343 $[=1535.272$ $+0.071]$	603.7818	996.1034	1105.601 $[=1105.858$ $-0.257]$	717.1869	-350.9387 $[=-350.9837$ $+0.0450]$	-227.6614
	3^{-13}	603.7818 $[=598.3338$ $+5.4480]$	996.1034 $[=996.0530$ $+0.0504]$	393.6204	646.2558	717.1869 $[=717.4571$ $-0.2702]$	465.1920	-227.6614 $[=-227.7103$ $+0.0489]$	-147.6819
A25-90 $(50, 0.9)$	3^{-14}	1223.239 $[=1216.955$ $+6.284]$	2025.962 $[=2025.872$ $+0.090]$	795.7958	1314.407	1458.949 $[=1459.238$ $-0.289]$	946.4155	-463.0916 $[=-463.1415$ $+0.0498]$	-300.4207
	3^{-13}	795.7958 $[=789.5330$ $+6.2628]$	1314.407 $[=1314.341$ $+0.066]$	518.4778	852.7658	946.4155 $[=946.7212$ $-0.3057]$	613.8953	-300.4207 $[=-300.4757$ $+0.0549]$	-194.8836

$n = 3$ is used in all analyses. The smallest element size of the coarse model, ne_0, is three times as large as that of the fine model.

Table 2. Mesh-independent ISSF ratio $K^{SLJ}_{\sigma_{ij},\lambda_1}/K^{SLJ*}_{\sigma_{ij},\lambda_1}$ and $K^{SLJ}_{\sigma_{ij},\lambda_2}/K^{SLJ*}_{\sigma_{ij},\lambda_2}$ obtained from the FEM stress in Table 1.

$SLJ/SLJ*$	e_0	Present method $K^{SLJ}_{\sigma_x,\lambda_1}/K^{SLJ*}_{\sigma_x,\lambda_1}$ $K^{SLJ}_{\sigma_x,\lambda_2}/K^{SLJ*}_{\sigma_x,\lambda_2}$ Mat. 1	Mat. 2	$K^{SLJ}_{\sigma_y,\lambda_1}/K^{SLJ*}_{\sigma_y,\lambda_1}$ $K^{SLJ}_{\sigma_y,\lambda_2}/K^{SLJ*}_{\sigma_y,\lambda_2}$	$K^{SLJ}_{\tau_{xy},\lambda_1}/K^{SLJ*}_{\tau_{xy},\lambda_1}$ $K^{SLJ}_{\tau_{xy},\lambda_2}/K^{SLJ*}_{\tau_{xy},\lambda_2}$	RWCIM $K^{SLJ}_{\sigma_{ij},\lambda_1}/K^{SLJ*}_{\sigma_{ij},\lambda_1}$ $K^{SLJ}_{\sigma_{ij},\lambda_2}/K^{SLJ*}_{\sigma_{ij},\lambda_2}$
A50 / A25	3^{-14}	0.761	0.761	0.761	0.761	0.761
		0.781	0.678	0.800	0.761	
	3^{-13}	0.761	0.761	0.761	0.761	0.780
		0.780	0.837	0.775	0.793	
A25-90 / A25	3^{-14}	1.004	1.004	1.004	1.004	1.003
		0.898	0.859	0.899	0.843	
	3^{-13}	1.004	1.004	1.004	1.004	0.891
		0.897	1.093	0.877	0.891	

SLJ: unknown model, $SLJ*$: reference model

When $0.15\,\text{mm} \le t_2 \le 0.9\,\text{mm}$ and $15\,\text{mm} \le l_2 \le 50\,\text{mm}$, the $C^{SLJ}_{\sigma_{ij0}}/C^{SLJ*}_{\sigma_{ij0}}$ is almost constant and varies from 0.9 to 1.1. It can be confirmed that the similar singular stress fields are formed in the range.

Figure 10 shows the critical ISSFs at the fracture, $K^{SLJ}_{\sigma c}/K^{SLJ*}_{\sigma c}$, in the range of $0.15\,\text{mm} \le t_2 \le 0.9\,\text{mm}$ and $10\,\text{mm} \le l_2 \le 50\,\text{mm}$. The solid line is the average $K^{SLJ}_{\sigma c}/K^{SLJ*}_{\sigma c}$. The $K^{SLJ}_{\sigma c}/K^{SLJ*}_{\sigma c}$ values are constant within about 10 % error.

5. Conclusion

In this paper, the ISSFs for the SLJ were calculated by changing the adhesive thickness t_2 and the overlap length l_2 and the similarity of the singular stress field of the SLJ was discussed. Then, it was shown that the debonding strength can be expressed as the constant value of the ISSF. The following conclusion can be drawn.

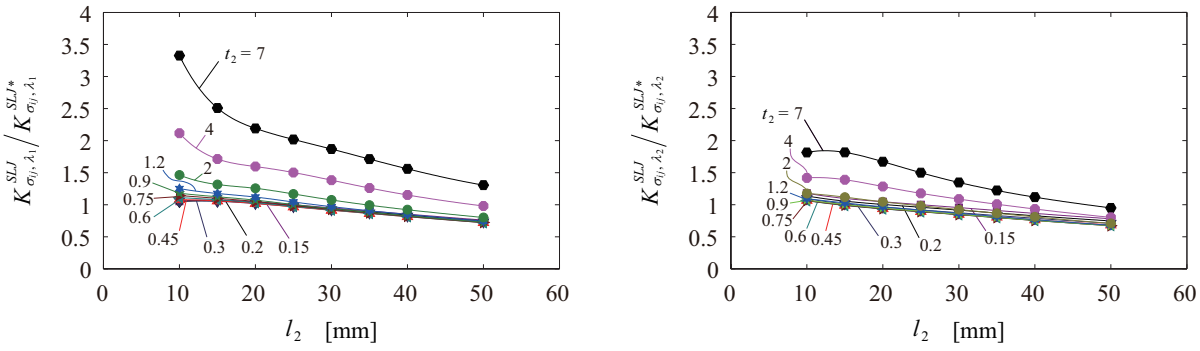

(a) $K^{SLJ}_{\sigma_{ij},\lambda_1}/K^{SLJ*}_{\sigma_{ij},\lambda_1}$ vs l_2. (b) $K^{SLJ}_{\sigma_{ij},\lambda_2}/K^{SLJ*}_{\sigma_{ij},\lambda_2}$ vs l_2.

Figure 8. Relation between $K^{SLJ}_{\sigma_{ij},\lambda_1}/K^{SLJ*}_{\sigma_{ij},\lambda_1}$, $K^{SLJ}_{\sigma_{ij},\lambda_2}/K^{SLJ*}_{\sigma_{ij},\lambda_2}$ and l_2.

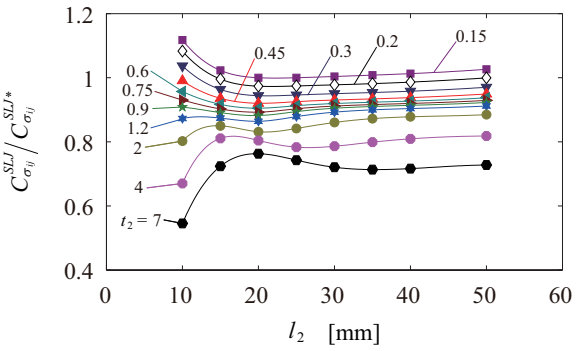

Figure 9. Relation between $C^{SLJ}_{\sigma_{ij}}/C^{SLJ*}_{\sigma_{ij}}$ and l_2.

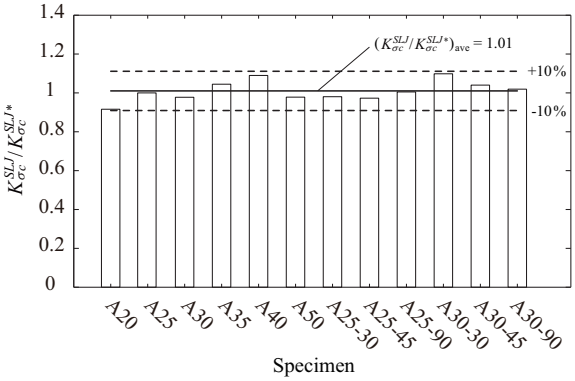

Figure 10. Debonding fracture criterion.

(i) The analysis method for calculating the ISSF is applied to the previous tensile test results of the SLJ composed of the aluminum alloy and the epoxy resin. It was found that the similar singular stress fields are formed in the range of 0.15 mm $\leq t_2 \leq$ 0.9 mm and 15 mm $\leq l_2 \leq$ 50 mm in the case of the SLJ with 225 mm in total length and 7 mm in adherend thickness.

(ii) When the specimens are satisfied with 0.15 mm $\leq t_2 \leq$ 0.9 mm and 15 mm $\leq l_2 \leq$ 50 mm, the critical ISSFs at the fracture were constant within 10 % error.

(iii) It was found that the FEM stress can be divided to two FEM stresses by applying the unknown and reference models to different minimum element sizes. Two ISSFs for the SLJ can be obtained by using the divided FEM stresses.

References

[1] Qian, Z. and Akisanya, A. R., An experimental investigation of failure initiation in bonded joints, Acta Materialia, Vol. 46, No. 14 (1998), pp. 4895 - 4904.

[2] Mintzas, A. and Nowell, D., Validation of an H_{cr}-based fracture initiation criterion for adhesively, Engineering Fracture Mechanics, Vol. 80 (2012), pp. 13 - 27.

[3] Zhang, Y., Noda, N. -A., Wu, P. and Duan, M., A mesh-independent technique to evaluate stress singularities in adhesive joints, International Journal of Adhesion and adhesives, Vol. 57 (2015a), pp. 105 - 117.

[4] Zhang, Y., Noda, N. -A., Wu, P. and Duan, M., Corrigendum to "A mesh-independent technique to evaluate stress singularities in adhesive joints" [International Journal of Adhesion and adhesives, Vol. 57 (2015), pp. 105 - 117], International Journal of Adhesion and adhesives, Vol. 60 (2015b), pp. 130.

[5] Chen, D. H. and Nisitani, H., Intensity of singular stress field near the interface edge point of a bonded strip, Transactions of the Japan Society of Mechanical Engineers, Series A, Vol. 59,No. 567 (1993),pp. 2682 - 2686 (in Japanese).
[6] Li, Y. L., Hu, S. Y., Munz, D. and Yang, Y. Y., Asymptotic description of the stress field around the bond edge of a cylindrical joint, Archive of Applied Mechanics, Vol. 68, No. 7-8 (1998), pp. 552 - 565.
[7] Koguchi, H., Distribution of displacements and stresses near stress singularity field at a vertex in three-dimensional bonded structures, Transactions of the Japan Society of Mechanical Engineers, Series A, Vol. 66, No. 648 (2000), pp. 1597 - 1605 (in Japanese).
[8] Noda, N. -A., Shirao, R., Li, J. and Sugimoto, J., Intensity of singular stress at the end of a fiber under pull-out force, Transactions of the Japan Society of Mechanical Engineers, Series A, Vol. 72, No. 721, (2006), pp. 1397 - 1404 (in Japanese).
[9] Noda, N. -A., Miyazaki, T., Uchikoba, T., Li, R., Sano, Y. and Takase, Y., Convenient debonding strength evaluation based on the intensity of singular stress for adhesive joints, Journal of the Japan Institute of Electronics Packaging, Vol. 17, No. 2 (2014), pp. 132 - 142 (in Japanese).
[10] Miyazaki, T., Noda, N. -A., Uchikoba, T., Li, R. and Sano, Y., Proposal of a Convenient and Accurate Method for Evaluation of Debonding Strength, Transactions of the Society of Automotive Engineers of Japan, Vol. 45, No. 5 (2014), pp. 895 - 901 (in Japanese).
[11] Noda, N. -A., Miyazaki, T., Li, R., Uchikoba, T. and Sano, Y., Debonding strength evaluation in terms of the intensity of singular stress at the interface coner with and without fictitious crack, International Journal of Adhesion and adhesives, Vol. 61 (2015), pp. 46 - 64.
[12] Miyazaki, T., Noda, N. -A., Wang, Z. and Sano, Y., Analysis of intensity of singular stress field for bonded cylinder in comparison with bonded plate, Transactions of the JSME (in Japanese), Vol. 81, No. 829 (2015), DOI: 10.1299/transjsme.15-00210.
[13] Miyazaki, T., Noda, N. -A., Li, R., Uchikoba, T. and Sano, Y., Debonding criterion for single lap joints from the intensity of singular stress field, Journal of the Japan Institute of Electronics Packaging, Vol. 16, No. 2 (2013), pp. 143 - 151 (in Japanese).
[14] Nisitani, H., Teranishi, T., Highly accurate values of K_I and K_{II} of axially symmetrical cracked body subjected to tension obtained by FEM, Damage and fracture mechanics VI, (2000), pp. 461 - 469, WIT Press.
[15] Nisitani, H., Teranishi, T.. K_I of a circumferential crack emanating from an ellipsoidal cavity obtained by the crack tip stress method in FEM, Engineering Fracture Mechanics, Vol. 70 (2002), pp. 579 - 585.
[16] Park, J. -H., Choi, J. -H. and Kweon, J. -H., Evaluating the strength of thick aluminum-to-aluminum joints with different adhesive lengths and thicknesses, Composite Structures, Vol. 92 (2010), pp. 2226 - 2235.